

N-body Simulations of Mergers based on Giant Radio Galaxy Fornax A

Elko Gerville-Reache¹, Jeffrey Kenney¹, and Shashank Dattathri¹

¹Yale University Department of Astrophysics

ABSTRACT

The giant elliptical radio galaxy Fornax A is dominated by complex kinematics and an irregular molecular gas distribution indicating it experienced one or more violent galactic scale mergers in the past ~ 1 Gyr. Its proximity and brightness makes it an ideal candidate for understanding the complicated dynamics between stellar matter and gas in the context of galaxy mergers. In this thesis work, we ran a set of N-body galaxy merger simulations of collisionless stellar particles between a large Hernquist spherical galaxy and a smaller rotating disk. The simulation assumed a mass ratio of 10:1 between the galaxies and investigated the effects of collisions with high radial components and different disk inclinations.

Keywords: N-Body simulations, Galaxy Mergers, Fornax A

1 INTRODUCTION

Fornax A (NGC 1316) is a giant elliptical radio galaxy located in the outer edges of the Fornax galaxy cluster at a distance of 20.8 ± 0.5 Mpc. The brightest member of its cluster, Fornax A is also the third brightest nearby radio source at 259 Jy after Centaurus A (NGC 5128) and M87 (Iodice et al., 2017). NGC 1316 is characterized by complex morphological features with strong evidence pointing to a rich history of merger events. The galaxy has been studied extensively in optical and infrared wavelengths, revealing the complicated morphology that makes up NGC 1316. Two distinct components can be mapped, with the main galactic body consisting of a spheroid with dust and gas scattered throughout. This central spheroid contains highly irregular molecular gas (CO) clouds with high velocity dispersions and disrupted kinematics (Kenney, 2013). Numerous long, tidally compressed filaments and blobs are scattered radially throughout the core (see Figure 1), strongly suggesting one or more recent mergers took place ~ 1 Gyr ago, and is evidence Fornax A is still in the process of relaxing (Iodice et al., 2017). At large radii $\sim 33 \leq R \leq 200$ kpc from the galaxy center, the galaxy consists of a vast stellar envelope with dust patches and elongated loops of stellar matter (Iodice et al., 2017). Schweizer (1980) provided the first detailed account of Fornax A in literature, identifying loops L1-L5 surrounding the galactic nucleus of the galaxy, of which L5 dominates in size. A giant HII region was also detected south of the galactic center. Later using the ESO VST, Iodice et al. (2017) discovered numerous fainter loops L6-L9 in the outer edges of the stellar envelope. These loops are likely tidally distorted, expelled stellar matter disrupted by a violent merger, and are still in the process of assembling into a relaxed state. Integrated g-r color analysis revealed a wide range of colors in the galaxy, with loops L2 and L3 notably being ~ 0.13 mag bluer than the average color of Fornax A, indicating possible external origin. From derived M/L ratios Iodice et al. (2017) estimated a total mass of $5.2 \leq M \leq 8.3 \times 10^{11} M_{\odot}$. Being situated in the Fornax cluster, NGC 1316 is surrounded by other smaller galaxies, of which NGC 1317 appears very close in projection to NGC 1316. Yet due to the absence of tidal distortions in NGC 1317's disk it is reasonable to assume they have not interacted strongly at this present time (Richtler et al., 2014).

The CO gas distribution in the central region $r \sim 6$ kpc has a highly irregular spatial distribution and highly disturbed kinematics (Maccagni, F. M. et al., 2020; Kenney, 2023). Many of the molecular clouds adjacent to each other have large differences in velocity, and in some regions there are multiple clouds along the line of sight, with velocities differing by 100-500 km/s (see Figure 2). These indicate that the molecular gas is not distributed in a thin rotating disk but rather has a non-planar configuration with clumps on irregular orbits. Kenney et al. (2023) propose this is largely due to the gas clumps from a disrupted accreted galaxy settling into the new gravitational potential. In support of this argument, 95% of the CO flux is located in 2 opposing quadrants, unlike a gas disk, but resembling merger debris from mergers with large radial components. Early type galaxies such as Fornax A typically have little to no gas, further supporting most of it came from in-fall during a violent merger. However, gas also experiences multiple non-gravitational forces, including frictional forces between the gas components of the 2 galaxies, and shocks and winds driven by radio jet outbursts. Collisions between the gas particles further average out random motions over time, creating complex kinematics. We wish to learn how much of the irregularities in the spatial distribution and kinematics of the molecular gas can be understood by gravitational effects alone during a merger, and how much is due to non-gravitational effects on the gas. Thus we investigate simple galactic merger simulations consisting only of collisionless stellar particles to see which of the irregular CO features present in Fornax A might be caused solely by gravitational effects.



Figure 1. HST image of central 2' (10 kpc) of NGC 1316, processed by unsharp masking to emphasize dust extinction features. The dust is strongly correlated with CO emission, and shows the disturbed state of the cold dense ISM. The image has been rotated CCW by 90° to align the gas features with the position v velocity diagram of Figure 2. Figure adapted from NASA, ESA, and The Hubble Heritage Team (STScI/AURA), 2005.

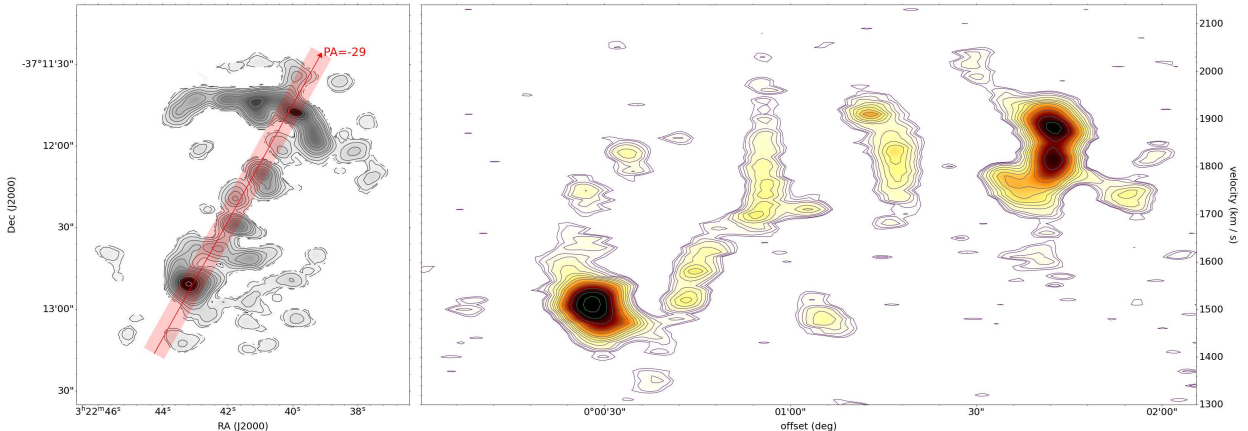


Figure 2. Left panel: Intensity plot of molecular CO gas found in the central core of NGC 1316, its distribution closely following the dust features visible in Figure 1. The red line displays the main axis along the gas where the positions and velocities along the line of sight were measured. Right panel: Position v. line of sight velocity diagram corresponding to the gas along the red line. Figure adapted from Kenney et al., 2023.

2 SETTING UP AND RUNNING N-BODY SIMULATIONS OF GALAXIES AND MERGERS

For this investigation, we ran a set of galactic merger simulations between a spheroidal early-type galaxy and a disk galaxy with a 10:1 mass ratio. This mass ratio is based on observed total gas mass estimates of $\sim 10^9 M_\odot$ in Fornax A and typical stellar to gas mass ratios in spiral galaxies, suggesting the perturber galaxy likely had mass of $\sim 10^{10} M_\odot$ (Lanz et al., 2010). The early type galaxy representing Fornax A was modeled from a Hernquist density profile, which benefits from having spherical symmetry and thus greatly simplifies calculations. Simple axisymmetric rotating disks of particles, on the other hand, are much harder to model in equilibrium and were modelled using the Agama python package (Vasiliev, 2018). A total of three different simulation runs were modeled, with varying disk inclinations and impact parameters to try and understand how these might impact the molecular gas distribution in the merger remnant.

This thesis project focuses on understanding how to properly set up and run N-body simulations of galaxies and simulate mergers between them. The entire project and simulation analysis was written in Python with the exception of the disk galaxy model code adapted from Vasiliev (2018). The following sections 2.1-2.5 describe the mathematical theory and code implementation of N-body simulations as well as the methods of generating self-gravitating N-body models for each galaxy. The process of assessing a particular model's equilibrium in isolation before merging them is also discussed. Thus the majority of this work is on running N-body simulations rather than applying them to Fornax A, which would require more complex simulations.

2.1 The N-Body Problem

The N-body problem in astrophysics attempts to solve the motion of N bodies through space under their mutual gravitational attraction. For a system comprising of $N = 2$ bodies, there exists an analytical solution to their trajectories, allowing for accurate predictions of their positions and velocities at some future time t . The conical orbit sections and Kepler's laws are derived from this solution. The problem arises when $N \geq 3$, where the chaotic nature of the system results in no solvable analytic solution. Chaotic systems are not random in nature but instead are characterized by having a unique solution for every set of initial conditions. These systems are highly sensitive to changes in initial conditions, where seemingly small fluctuations can lead to highly divergent solutions. For small numbers of N , constraints can be made to approximate the trajectories accurately. Yet when studying globular clusters or galaxies, $N \simeq 10^6 - 10^{11}$, therefore complicating calculations a great deal. Thus, the lack of an analytical solution requires a numerical approach for predicting the orbits of systems with large N . Numerical approximations integrate the equations of motion of each particle in discrete timesteps Δt , and then recursively uses the previous set of positions and velocities to compute the next timestep. Consequently, the accuracy of these calculations are highly dependent on the size of Δt as well as the number of timesteps, since integrating longer into the future will accumulate more numerical errors.

2.2 N-Body Code

In this simulation, all particles are assumed to be collisionless, baryonic, stellar masses. Extragalactic systems can be characterized by their relaxation time, which measures how long it takes for some star's trajectory to be significantly perturbed by the other stars. In a system of N particles, $t_{\text{relax}} \simeq \frac{N}{8 \ln N} t_{\text{cross}}$, where the crossing time is defined as $t_{\text{cross}} = R/v$, or the average time for a star to travel across the system. For a typical galaxy with $N \simeq 10^{11}$ and $t_{\text{cross}} \simeq 10^8$ years, the relaxation time is much greater than a typical simulation timescale, and collisions can therefore be ignored completely. Galaxies are a few hundred crossing times old and therefore can be approximated as collisionless systems even during a violent merger event. In globular clusters the crossing time and number of stars are much lower, so stellar encounters may be of importance over the lifetime of the cluster (Binney and Tremaine, 1987). The dark matter halo, central bulge and black hole, as well as gas particles, which are important components of galaxies are completely omitted in these simulations. These approximations are necessary to keep N low enough to run the simulation on a personal computer, as well as ensure the system is collisionless. Gas particles are collisional by nature, and require more advanced techniques such as fluid simulations to properly simulate. The N-body code therefore assumes the only force operating on the particles is from their mutual gravitational attraction. Given a set of particles with initial positions and velocities, the next timestep is computed by brute force using the leap-frog algorithm. For each particle, the gravitational acceleration acting onto it must be calculated by summing up the individual particle-particle contributions from all the other stars. Thus, the gravitational acceleration g_i onto a particle p_i can be expressed as a sum over all the other particles j , where r represents the particle's positional vector in 3D space and ϵ , the softening length (equation 1). ϵ ensures the effects of close encounters are smoothed, and that dividing by zero does not occur. Its value is determined by the number of particles based on a relation derived by Dehnen (2001) for Plummer spheres (equation 2), and also serves as the simulation resolution. Close encounters between particles with a distance smaller than ϵ cannot be resolved.

$$g_i = G \sum_j^N \frac{m_j [r_j - r_i]}{[|r_j - r_i|^2 + \epsilon^2]^{3/2}} \quad (1) \quad \epsilon = 0.017 \left[\frac{N}{10^5} \right]^{-0.23} \quad (2)$$

Once the acceleration is computed, the positions and velocities of the next timestep can then be calculated using the standard kinematic equations of motion. The leap-frog algorithm computes the velocities and positions at interleaved timesteps where the velocities are calculated at half timesteps before and after computing the new positions. This creates a 'kick,' 'drift,' 'kick' method conserving Energy to the second order and is a good trade-off between accuracy and computational efficiency. The new positions are then used to calculate a new set of accelerations, continuing the cycle endlessly. The leap-frog method is also time reversible, making it a standard choice in most N-body codes.

$$v_{t+\frac{1}{2}} = v_t + g_t \frac{\Delta t}{2} \quad (3) \quad x_{t+1} = x_t + v_{t+\frac{1}{2}} \Delta t \quad (4)$$

Direct particle-particle summation may be the most accurate class of N-body simulations, but comes with a heavy computational price of $O(N^2)$ time, placing an upper limit on the number of particles in the simulation on the order of $\sim 10^4$. The integrator saves the phase space coordinates x, y, z, v_x, v_y, v_z , and potential $\phi_i = \frac{1}{m_i} \sum_j \frac{G m_j}{|r_j - r_i + \epsilon|}$ of each particle every 10 timesteps as a $N \times 7$ matrix. Moreover, in all simulations runs model units are assumed, where the gravitational constant G , the total system mass M , and scale length α are all set equal to 1. The models can then easily be scaled relative to each other by multiplying the initial phase space coordinates and masses by scalar quantities. Furthermore, in these models each particle represents a large collection of stars since the simulations ran for this investigation are of the order $N \propto 10^4$, or many orders of magnitude less than real galaxies. Thus, the greater the number of particles, the higher the simulation resolution. Certain features seen in merger remnants such as stellar shells require large numbers of particles to resolve. As such, simulating millions of particles requires both heavy computational power from super-clusters and more efficient N-body integration schemes.

2.3 Generating Initial Conditions

In attempting to model NGC 1316, a spherical Hernquist density profile was chosen, notable for its spherical symmetry and analytic solution. Its mass density follows equation (5), where M represents the total mass of the system and α , the scale length or the radius at which the density starts to drop off. Integrating the mass density with respect to r computes the enclosed mass at a given radius R , given by equation (6). This distribution is shown in Figure 3 (left panel), overplotted against the analytical enclosed mass distribution for a Hernquist sphere.

$$\rho(r) = \frac{M\alpha}{2\pi r(r+\alpha)^3} \quad (5)$$

$$M_{enc}(R) = 4\pi \int_0^R r^2 \rho(r) dr \quad (6)$$

Inverse transform sampling is then used to generate a set of radii that follow the Hernquist density profile. Separating these radii into their 3-dimensional x, y, z initial positions is made simple by taking advantage of the profile's symmetry using spherical coordinates.

$$x = r \sin\theta \cos\phi \quad (7)$$

$$y = r \sin\theta \sin\phi \quad (8)$$

$$z = r \cos\theta \quad (9)$$

Spherical symmetry allows for the azimuthal angle to be uniformly distributed in the range $\phi \in [0, 2\pi]$. The radial angle must be more carefully generated since uniformly generating θ would result in over-densities at the poles. Thus, $\theta = \arccos[x]$, where x is uniformly distributed over the interval $[-1, 1]$. For a system of N particles, N number ϕ and θ angles are generated. Having generated a set of particles following the Hernquist distribution, their velocities must be computed next. When assigning velocities to each particle, great care must be taken to ensure that all are bounded to the galaxy if the system is to be in equilibrium. For a Hernquist sphere, the number of stars at any given Energy level is described by the distribution function $f(\mathcal{E})$, where \mathcal{E} and Ψ are the relative Energy and relative potential given by $\mathcal{E} \equiv -E = \Psi - \frac{1}{2}v^2$ and $\Psi \equiv -\Phi$. $f(\mathcal{E})$ is defined to be 0 for all $\mathcal{E} < 0$ and non-negative for $\mathcal{E} \geq 0$ (Binney and Tremaine, 1987).

$$f(\mathcal{E}) = \frac{1}{\sqrt{8\pi^2}} \int_0^{\mathcal{E}} \frac{d^2\rho}{d\Psi^2} \frac{d\Psi}{\sqrt{\mathcal{E}-\Psi}} \quad (10)$$

$$\Phi = -\frac{GM}{r+\alpha} \quad (11)$$

In this paper, all Energy and potential calculations follow relative convention. To compute the magnitude of the velocity for a given particle, it is critical that its magnitude is less than the escape velocity at that position, defined as $v_{esc} = \sqrt{2|\Psi|}$. It can be shown that the probability of a particle p_i having some velocity v is proportional to $v^2 f(\Psi_i - \frac{1}{2}v^2)$, where Ψ_i is the potential of the particle and v is some velocity in the range $[0, v_{esc}]$ (Binney and Tremaine, 1987). Integrating this probability density function over v for each particle across its range of acceptable velocities generates a cumulative distribution function, which can be used to assign a velocity magnitude to each particle using inverse transform sampling. This method ensures each particle is bound to the system by only choosing velocities within the allowed Energy levels. Similarly to the position components, the 3-dimensional v_x, v_y, v_z components of the velocities are assigned using spherical coordinates. Having generated the initial phase space coordinates of our N-body model, the individual particle masses, m are initialized using the equation $m = \frac{M}{N}$, where M is the total galaxy mass and N the total number of particles. This assumes the total mass of the galaxy is distributed evenly across each particle. The galaxy generation function outputs a $N \times 7$ matrix file containing the positions, velocities, and masses of the galaxy. In Figure 3 below, the enclosed mass distribution and distribution function of the N-body galaxy model is plotted against the analytical distributions to ensure they agree.

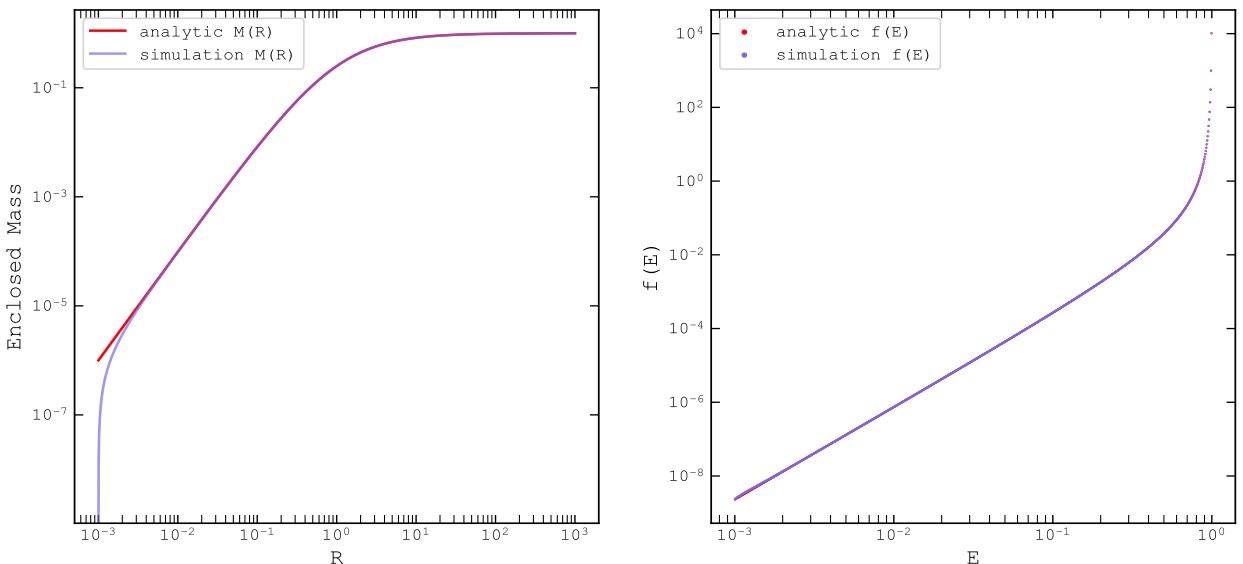


Figure 3. Left panel: Enclosed mass distribution $M(R)$ v. radius compared to the analytical enclosed mass distribution for a Hernquist sphere. Right panel: Plots of the analytical and simulation Energy Distribution Functions. The simulation distributions agree very well with the analytical expressions.

2.4 Testing Initial Conditions

Once suitable initial conditions are generated, as demonstrated in Figure 4, it is important to ensure the galaxy behaves as expected in isolation. Interactions between galaxies fundamentally alter the structure and Energy of the galaxies, thus it is important that with no external forces present, the galaxy stays in equilibrium. The initial phase space coordinates and masses are loaded into python arrays, and fed into the N-body integrator function, which also requires the number of timesteps and Δt as arguments. The softening length is automatically calculated based on the number of particles in the simulation. The N-body algorithm computes the positions, velocities, and potential of the particles for each timestep using the integration scheme described in section 2.2 and saves them as simulation snapshots. Once completed, the output files are loaded back into python and run through the analysis pipeline. The total Energy \mathcal{E} is computed from the velocities and potential, and plotting the histogram of this distribution shows the Number of particles at a given Energy level, $N(E)$. We can also use the analytical model once again to verify the results of the simulation, given by the equation $N(E) = f(E)g(E)NdE$, where $g(e)$ is the density of states (Binney and Tremaine, 1987). A galaxy in equilibrium should not deviate from the analytical curve after many timesteps of integration. Figure 5 (left panel) shows the normalized distribution of Energies $N(E)$ for the start and end times of the simulation run. The distributions closely agree with the analytical model, with the curve corresponding to $t = 2000$ only slightly deviating from the expected analytical values. This confirms that in isolation, the galaxy model is in equilibrium, giving us a control for simulating mergers.

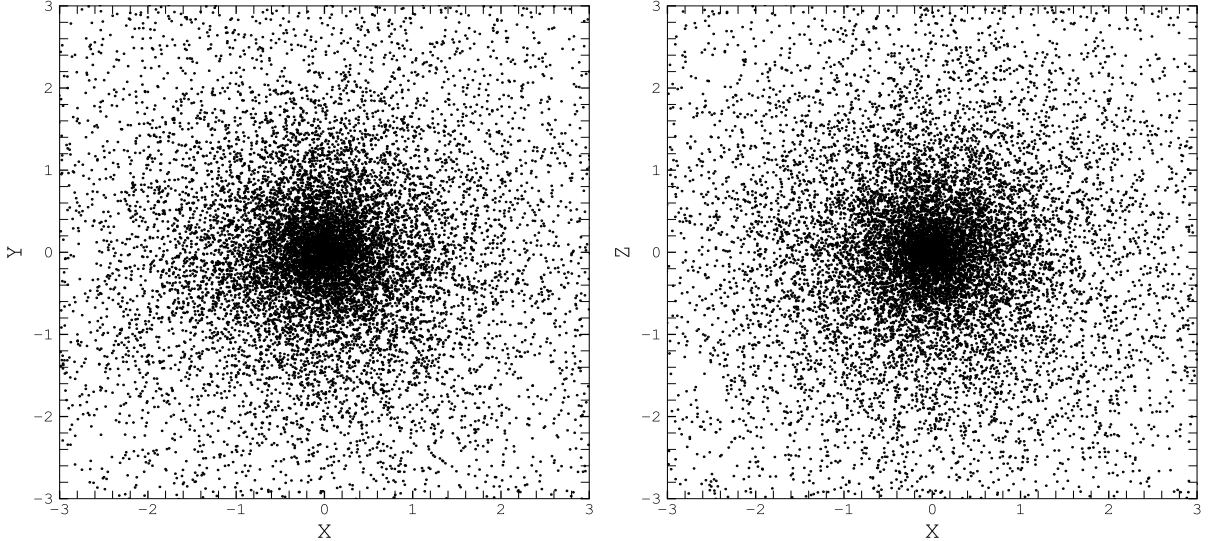


Figure 4. Various orthogonal projections of a Hernquist model initial positions with 20,000 particles, mass $M = 1$, and scale radius $\alpha = 1$. The galaxy's spherical symmetry is apparent across the different projections.

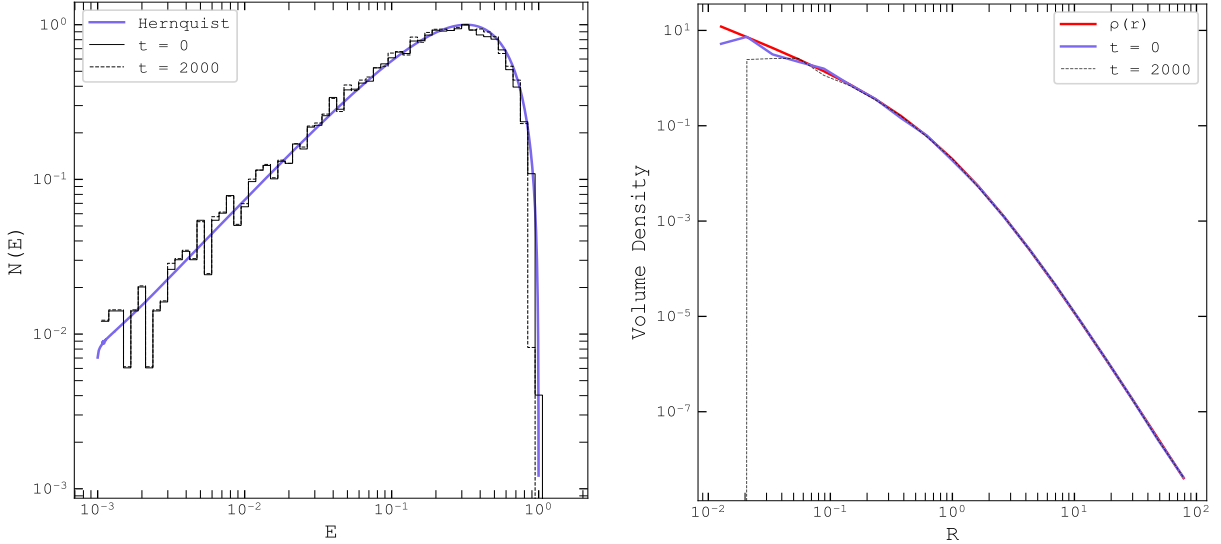


Figure 5. Left panel: $N(E)$ distribution of a test Hernquist model in isolation at timesteps $t = 0$ and $t = 2000$ overplotted with the analytical distribution of Energies. After 2000 iterations, the distribution of Energies still closely follows the analytical model and has not deviated significantly from the initial Energy distribution. Right panel: Density of the Hernquist model at the start and end of the simulation run overplotted against the analytical $\rho(r)$ distribution. At $t = 2000$, the density drops off from the expected value at $R \simeq \epsilon$ which is to be expected since the softening length sets the simulation resolution.

2.5 Perturber Galaxy

The perturbator galaxy was modeled as a single component disk galaxy, without a dark matter halo or central bulge and black hole to keep N sufficiently low. The gas component inherent to spiral galaxies was also left out due to the collisionless constraint of our simulation. Initial conditions were generated with the Agama python package (Vasiliev, 2018) using the SelfConsistentModel class, which supports building multiple component models using different potentials and distribution functions (DF). A 'Quasi-Isothermal' disk potential and distribution function was chosen to model the galaxy, with a surface density $\Sigma_0 = 0.63$, a disk radius $R_d = 0.9$, a scale height $H_d = 0.15$, and a radial velocity dispersion of $\sigma_r \in [0.21, 2.35]$. These values were optimized to keep the disk as stable as possible, with the Toomre stability parameter, Q in mind. For a stellar disk, this is defined as:

$$Q_{star} = \frac{\sigma_R \kappa}{\pi G \Sigma} \quad (12) \quad \kappa^2 = 2 \frac{v}{R} \left[\frac{v}{R} + \frac{dv}{dR} \right] \quad (13)$$

with κ defined as the epicyclic frequency (Binney and Tremaine, 1987). For a stable disk in equilibrium, $Q > 1$. Agama samples the DF and generates a set of initial phase space coordinates which can then be used as our perturber galaxy. Disk galaxies however are numerically unstable and very sensitive to initial parameters, with effects such as disk heating, or the gradual growth of random velocities, and accumulation of numerical errors causing the initial disk to expand radially (Binney and Tremaine, 1987). Integrating our model in isolation produces noticeable disk heating, with the initial thin disk morphing into a thicker disk, displayed in the left panel of Figure 6. Thicker disks have the advantage of being much more stable numerically, despite being physically less realistic. Yet after many timesteps, all the particles in the disk are still bound and self-gravitating in some quasi-equilibrium state. Plotting a log distribution of the Energies (Figure 6, right) across 2000 timesteps reveals acceptable convergence between the initial state and after numerous galaxy rotations, indicating the disk model is self-gravitating and confirming quasi-equilibrium. The Hernquist model Energy curve is also plotted for reference, and is notable for having a much broader range of acceptable Energies than a disk in equilibrium.

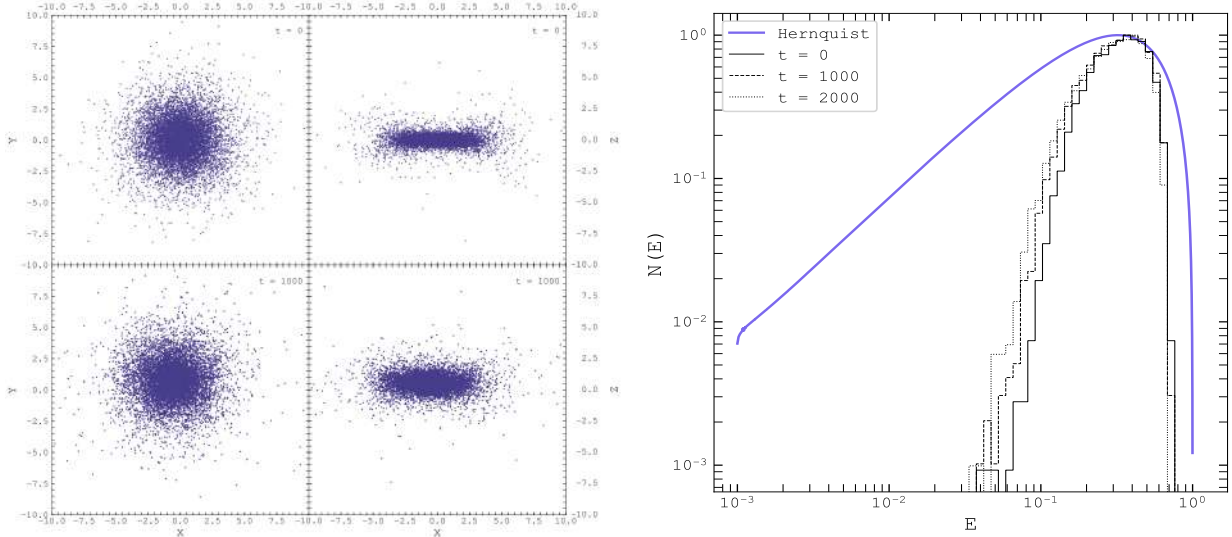


Figure 6. Left panel: xy and xz projections of timesteps $t = 0$ and $t = 1,000$ of the disk galaxy evolving in isolation. There is obvious disk bulging from instabilities however the system is self-gravitating and in quasi-equilibrium. Right panel: $N(E)$ distribution of a Hernquist profile overplotted with the $N(E)$ distribution of the disk galaxy in isolation at timesteps $t = 0, 1,000$, and $2,000$. Despite small fluctuations, the curves mostly converge, indicating the disk galaxy is self-gravitating.

2.6 Simulation Convergence

Because of heavy computational time, it is important to investigate the dependence on initial distances between the satellite and host galaxies. While placing the perturber many scale radii away from the host galaxy is more physically accurate, it would greatly increase computational time during the lead-up to the merger. Too small an initial separation could heavily bias the results leading to greater divergence between small differences in initial conditions. To choose an optimal consistent starting point a simple 10:1 merger was simulated, where a Hernquist sphere was placed at rest on the origin in a radial collision path with a disk galaxy 75 simulation units away. The disk was given a velocity of $v_x = -0.5$, corresponding to slightly less than the escape velocity at that distance. The velocity of the disk's center of mass was recorded at a distance of $x = 50$, and again at $x \approx \alpha$, when the galaxies start merging. A second test was conducted with an identical setup, but this time the disk was moved to a position of $x = 50$ and given the velocity recorded from the previous run at this position. Figure 7 (top panel) plots the magnitude of the center of mass velocity in the x direction for both galaxies, plotted over simulation timesteps. At a simulation time of $t = 50$, the two galaxies start to merge in both runs. The disk galaxy's v_{com_x} becomes increasingly negative until $t \approx 53$ where it crosses through the Hernquist galaxy center, and subsequently becomes pulled back towards the more massive Hernquist galaxy. The two runs agree quite closely showing the two simulations converged. From this test we can assume simulation results are irrespective of the initial separation distance up to $R \approx 50$ units, and all subsequent tests take on this initial distance.

3 PRELIMINARY RESULTS FROM THE MERGER SIMULATIONS

Based on the work done by Iodice et al. (2017), we investigated the merger between a giant, early type, spherical galaxy and a smaller disk galaxy with a mass ratio of 10:1. For all runs this mass ratio was assumed between the two galaxies. A total of three simulation runs were computed to more properly search simulation space, with varying simulation parameters. The mergers are characterized by either having a completely radial collision path or having a slight impact parameter, and the disk inclination was varied between edge-on or face-on. The choice for simulating mostly radial mergers is founded on the observed merger remnants seen in the inner spheroid of Fornax A, which are distributed radially along the galaxy. The spherical symmetry of the Hernquist sphere also greatly simplifies the initial setup, and allowed us to place the disk galaxy solely along the x -axis for radial mergers. All simulations were run on the Yale Astronomy department computer cluster which greatly sped up calculations and allowed for a massive increase in particles, and hence simulation resolution. All parameters for each simulation run are listed in Table 1.

3.1 Merger Initial Conditions

In all simulations, the Hernquist sphere was initiated with 13,000 particles, a mass of $M = 10$, and a scale radius of $\alpha = 2$. Each simulation adopts the Hernquist sphere's frame of reference, placing it at rest on the origin. The disk galaxy is generated with a total mass $M = 1$, and scale radius $\alpha \sim 3$ using the parameters outlined in section 2.5. Its center of mass is given an initial velocity pointing in the direction of the Hernquist galaxy with a magnitude slightly less than the escape speed. The first run investigated the effects of a radial, face-on merger with a total particle count of $N = 23,000$. The perturber disk consisted of 10,000 particles and was placed 50 simulation units away from the Hernquist sphere on the x -axis and its center of mass given an initial velocity $v_x = -0.5$. The disk inclination was completely parallel to the sphere for a face-on merger. In the next two runs, the particle count was increased for a higher resolution at the cost of slightly longer computational times. The second simulation run investigated the case of an edge-on, radial merger, this time with a total particle count of $N = 26,000$ distributed evenly across both galaxies. Similarly to the previous run, the disk was placed 50 units away with a COM velocity $v_x = -0.5$. In the third simulation run, the disk was setup to have a slight impact parameter by placing it 50 units away in the x direction and 10 units on the y direction. The inclination was set up to be edge-on and once again the COM velocity was set to $v_x = -0.5$. The galaxies also share an equal amount of particles totaling 26,000. For all mergers, the timestep was set to $dt = 0.05$, and the softening length determined by equation (2). Each simulation was evolved for approximately 5-7,000 timesteps, to properly assess the merging and relaxation process. The initial simulation configurations are shown in the lower panel of Figure 7. The COM position of the disk galaxy throughout the simulation is overplotted in each frame to show the trajectory of the perturber for each setup.

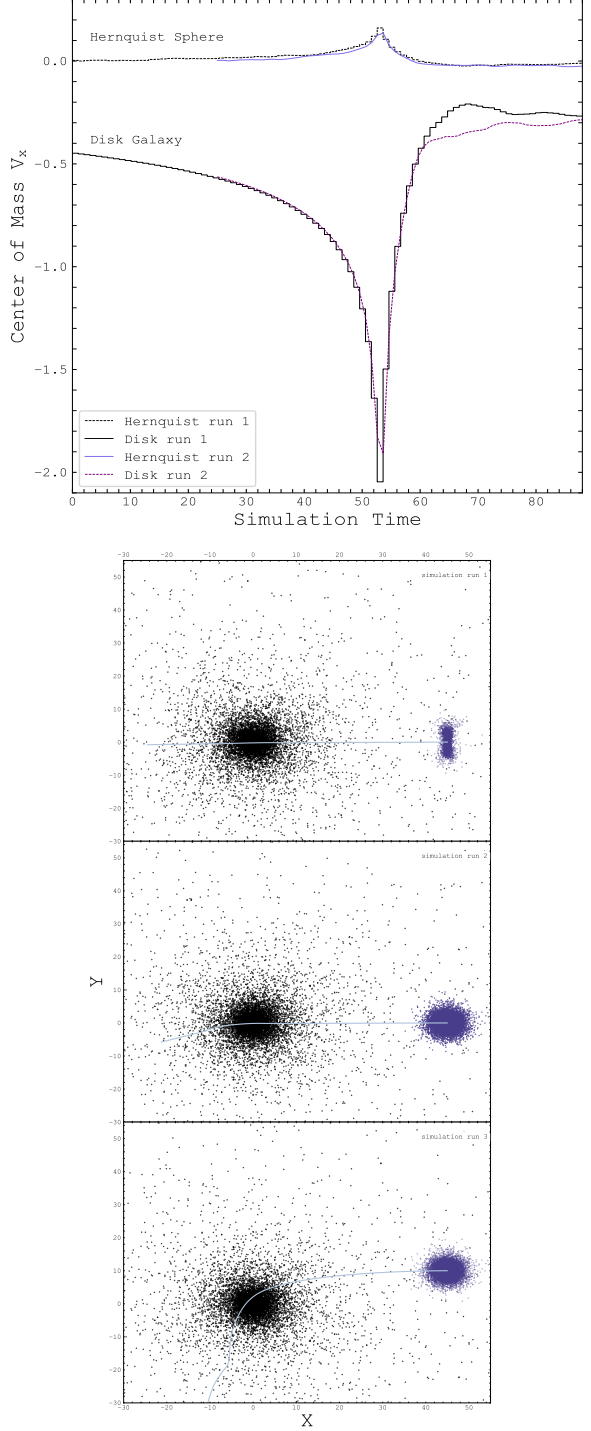


Figure 7. Top panel: Center of mass velocity in the x direction plotted over simulation time units for the two different 10:1 radial test mergers. The Hernquist and disk galaxy v_{com_x} are overplotted with the initial run plotted in black and the second simulation in color. The velocities agree with only slight differences during the merger event at $t \approx 60$ showing acceptable convergence. The effects of the 10:1 mass ratio are also of note, with the more massive Hernquist galaxy deviating only slightly from its initial center of mass. Bottom panel: Initial xy projections of the simulation setup for each run. The center of mass trajectory of the perturber galaxy is shown.

Simulation Run:	I	II	III
Hernquist Sphere			
M:	10	10	10
N:	13,000	13,000	13,000
α :	2	2	2
Initial Position:	origin	origin	origin
Disk Galaxy			
M:	1	1	1
N:	10,000	13,000	13,000
Initial Position [x, y, z]:	[50, 0, 0]	[50, 0, 0]	[50, 10, 0]
Initial COM Velocity [x, y, z]:	[-0.5, 0, 0]	[-0.5, 0, 0]	[-0.5, 0, 0]
Disk Inclination:	face-on	edge-on	edge-on

Table 1. Summary of the simulation parameters across all three runs, labeled I, II, and III.

3.2 Simulation Run 1

In the case of the face-on, radial merger the galaxies begin interacting strongly at a simulation time $t \sim 1,100$, where the disk begins to bunch up into an elongated spheroid (see timestep 1,100, Figure 9) before being ejected out the host galaxy at a high velocity. A distinctive conical shaped remnant is formed extending radially in the negative x direction, initially dispersing most of the disk particles. However, a portion of the disk is trapped under the gravitational potential and is seen oscillating radially in Figure 8 (left panel), with complex kinematics causing shells of particles overturning onto themselves. The disk particle's colors are mapped to the radial component of their velocities, clearly showing particles at similar x coordinates traveling in opposing directions. Yet this behavior is short lived with many of the central particles relaxing into the new potential after ~ 300 timesteps. Viewed from the yz plane (Figure 8, right panel), the axisymmetry of the disk is retained in the merger remnant yet the angular momentum from the disk rotation seems to have been lost. Many of the particles ejected out in the yz plane are also seen decelerating before reaching zero velocity and falling back into the host galaxy, as expected for a radial merger. Although interesting, the merger remnant does not match the more elongated filaments and clumps observed in Fornax A, suggesting the perturber galaxy likely collided more edge-on.

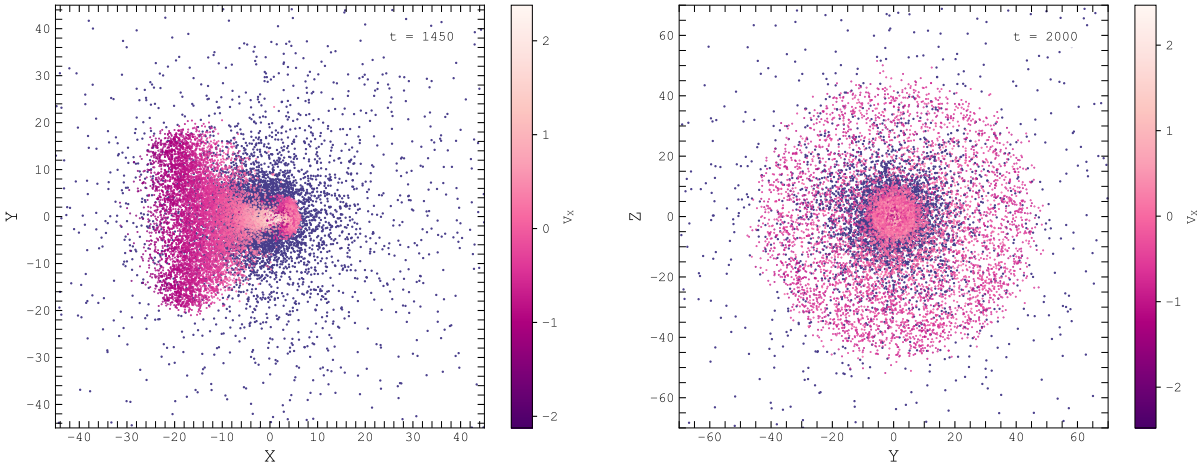


Figure 8. Left panel: xy projection of the face-on radial simulation at the height of the merger event. The disk particles are colored by their x velocity (radial) component. Right panel: yz projection at a slightly later time showing most of the disk particles relaxed in the center of the Hernquist sphere. The remainder of the particles extend radially out in the yz plane. The perturber particles are plotted on top of the host galaxy for clarity.

Phase space diagrams of the disk merger remnants are helpful tools for further comparing the simulation results to the merger remnant found in NGC 1316. A thin cross section of the disk remnant is chosen, typically along its major axis, and flattened into a 1-dimensional array. The component of their velocities along some line of sight, unit-vector of interest (v_{los}) is then computed through a dot product, allowing us to make position v. velocity diagrams of the simulation. Particles with positive v_{los} are moving away from the line of sight, while negative velocities indicate motion towards the 'observer'. Figure 9 displays a collection of time-series phase diagrams of simulation 1, for different line of sights and timesteps. Each phase space diagram also includes a plot of the disk remnant in real space along the line of sight for reference, as well as the cross section of interest, marked by the parallel pink lines. Right before the merger, the disk is rotating in the yz plane and traveling along the x direction, corresponding to $t = 1,000$ of Figure 9. All the particles have a positive v_{los} , traveling towards the Hernquist sphere at high velocity and away from the line of sight. Immediately after the impact ($t = 1,100$), the disk has become squished into a tight elongated spheroid by the potential of the Hernquist sphere, displayed in the topmost two plots of Figure 9. The kinematics of the merger debris is now more complex, with large differences in

velocity magnitude and direction for particles at similar positions, as they oscillate radially and form shells (see Figure 8). As the simulation progresses, most of the particles relax into a centrally concentrated merger remnant ($t = 1,550$) with the rest forming the conical tail apparent in Figure 8. The central spheroid displays symmetry in its phase space diagram corresponding to the particles settling into the new potential field. The final merger remnant projected on the yz plane is displayed on the last panel of Figure 9, showing a dense, centrally concentrated bulge in phase space with two long tails.

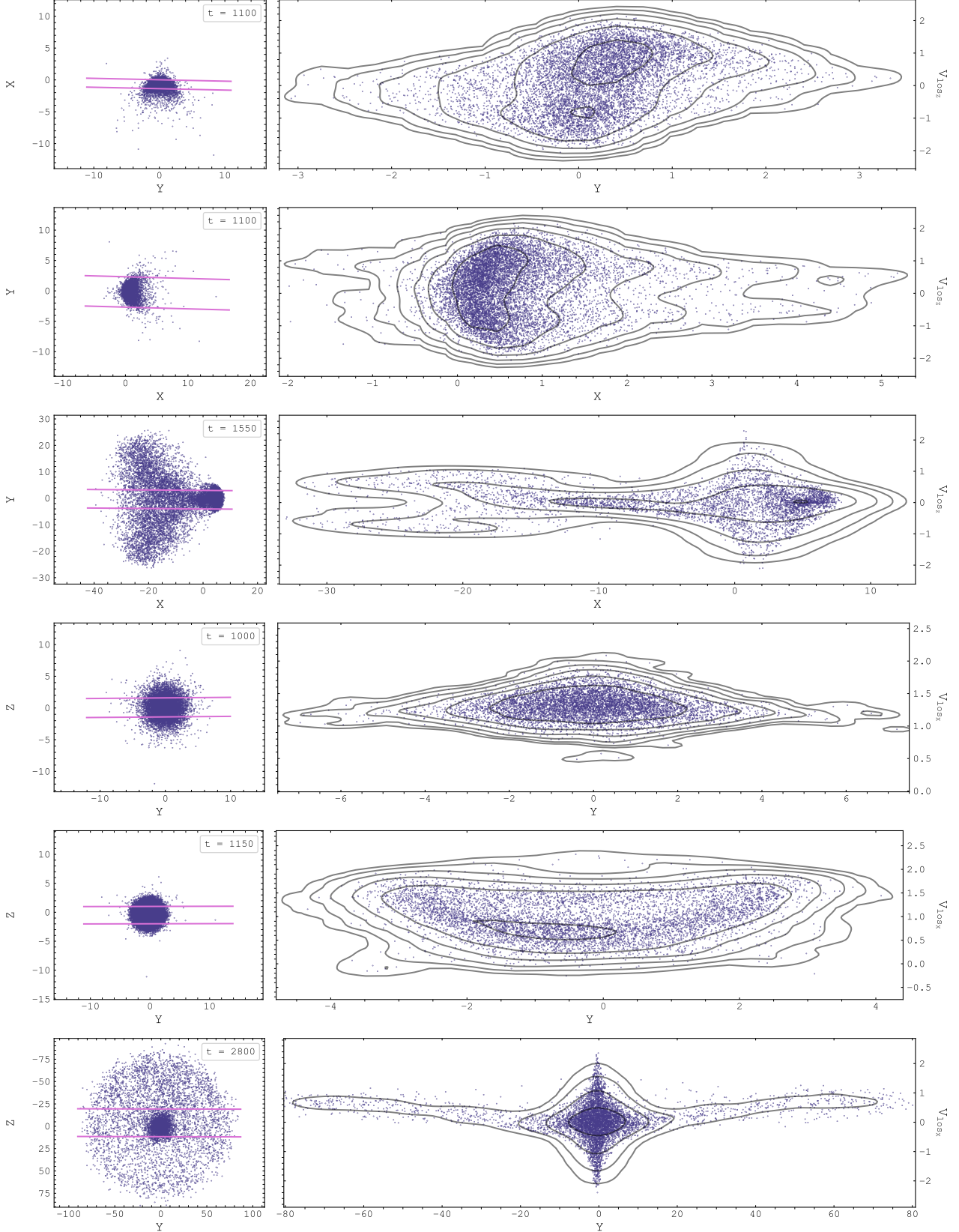


Figure 9. Position v. velocity diagrams of simulation 1 along varying lines of sight and at different timesteps. The top three panels were computed along the line of sight \hat{z} unit-vector, while the bottom three along the unit \hat{x} vector direction.

These two diverging tails have a slight inclination, starting with a positive v_{los} at large radii and slowly decreasing in magnitude before becoming negative towards the base of the tails. This corresponds to the outermost particles slowly losing kinetic Energy before coming at rest and eventually sinking back into central core.

3.3 Simulation Run 2

In the second simulation run, the satellite galaxy was rotated 90° to be edge-on to the Hernquist sphere, and began merging at $t \sim 1,000$. Unlike the face-on, radial merger which spread out axisymmetrically in the yz plane, the remnant formed throughout this simulation is more elongated with a distinct tail extending in the xy plane and curving towards the negative y direction. A small fraction of the particles are also seen forming a smaller, less dense tail in Figure 10, $t = 1,450$, traveling in the opposite direction. This smaller, tail-like structure is short lived, dispersing into a less dense, field of particles some ~ 200 timesteps later. This behavior is interesting as the satellite galaxy initially was traveling solely in the x direction, suggesting the merger remnant would oscillate back and forth on the x -axis. Yet the presence of the tail curving inwards can perhaps be explained by the rotational energy of the disk deviating the particles off-course, since the direction of the disk's rotation pointed in the same direction as the tail. Many of the particles in the tail have reached escape velocity, and travel at high speed away from the central spheroid throughout the simulation. This is apparent in Figure 16, right panel, which shows the final simulation snapshot of this run. The tail extends a couple hundred simulation units from the sphere with many of the particles having attained escape velocity.

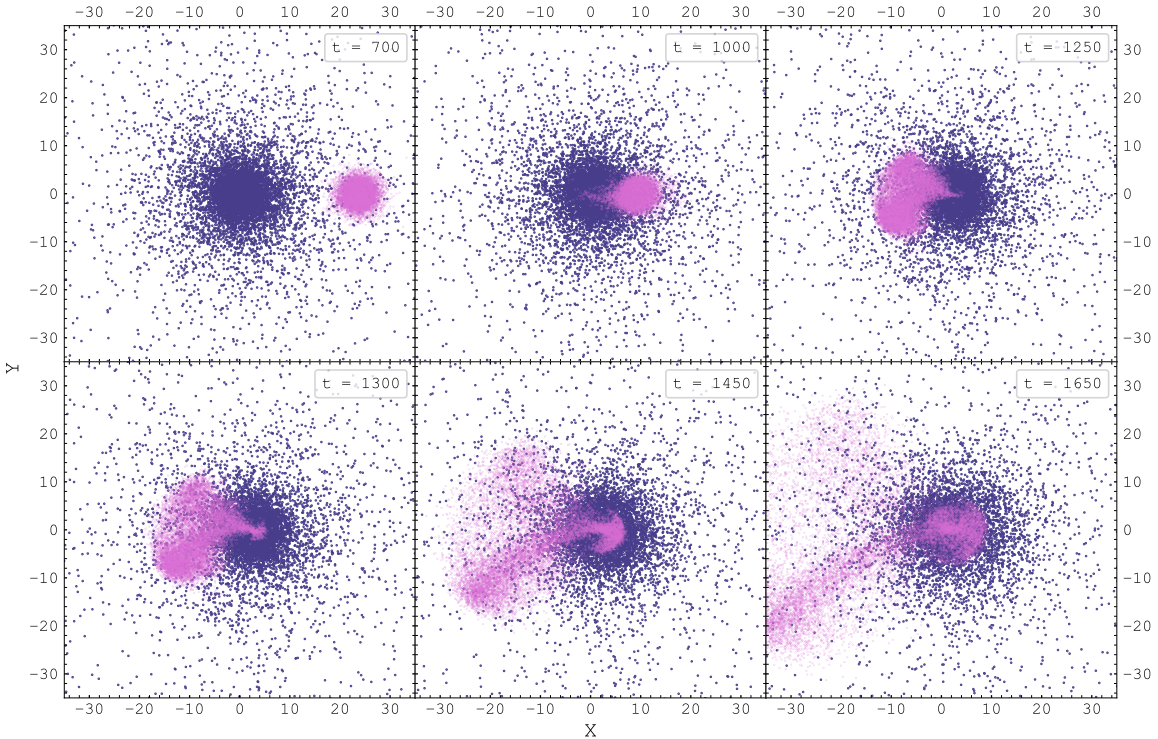


Figure 10. xy projection of the first 1,650 timesteps of simulation 2. The distinct twin tails forking out the central spheroid is apparent in the last two timesteps. The violent oscillations present in the central bulge are also in full view.

Rotating to the xz frame of reference (Figure 11), the dispersion of the particles is much tighter with the majority concentrated in the elongated tail extending in the negative x direction. The disk is stretched as it approaches the Hernquist sphere ($t = 1,000$), until it crosses the center and subsequently accelerates outwards with some vertical motions ($t = 1,250$). This increase in vertical velocity is apparent in Figure 15, right panel, where many of the particles are ejected upwards a couple times the disk scale height. The particles now closest to the center of the spherical galaxy are pulled back in and start to oscillate forming irregular, spherical shells of radius $r \sim 10$ units ($t = 1,650$). Particles near the center continue to oscillate violently in the core, before relaxing into a spheroidal remnant. In Figures 12-16, different simulation snapshot closeups of the central region are displayed, along with radial velocity information encoded within the color-map. This highlights the direction of travel of the different particles in the radial direction. Figure 14 is particularly interesting, with the large stellar shells in full view as they loop around the center of the spheroid. The disk debris seems to oscillate 3-4 times about the center of Hernquist galaxy before settling into a tight ball of particles. In timestep 5,000, corresponding to the end of the simulation, the central bulge of particles is now mostly spheroidal and has grown considerably ($r \sim 25$). Figure 16, right panel, also displays the last timestep of the simulation along with log histogram plots of the number density distribution of each galaxy. The Hernquist galaxy distribution seems mostly unaffected, its central density peak having deviated only slightly from the origin. On the other hand, the merger debris of the disk is much more irregularly spread out. The disk density is highest in the 'third quadrant' of the plot, in the direction of the tail.

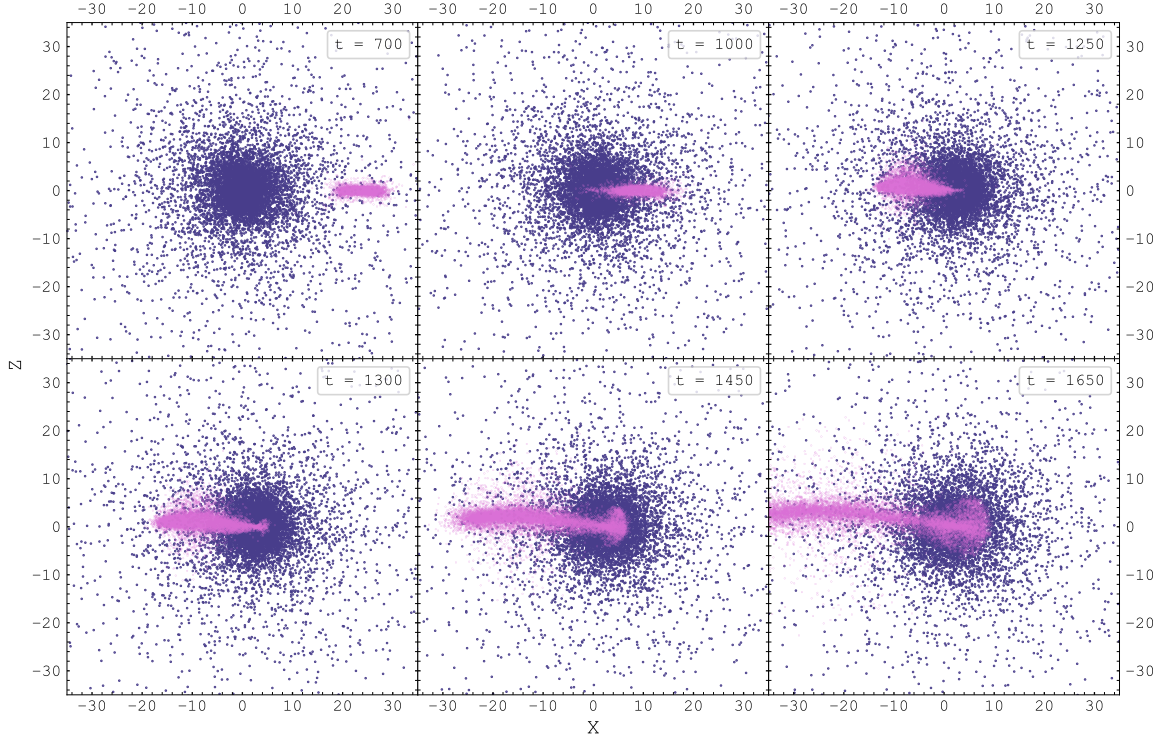


Figure 11. xz projection of the same timesteps as Figure 10. The merger remnant is clearly confined to the xy plane, with little to no vertical motions. The distinctive radial oscillations and shells are also apparent after $t = 1,300$.

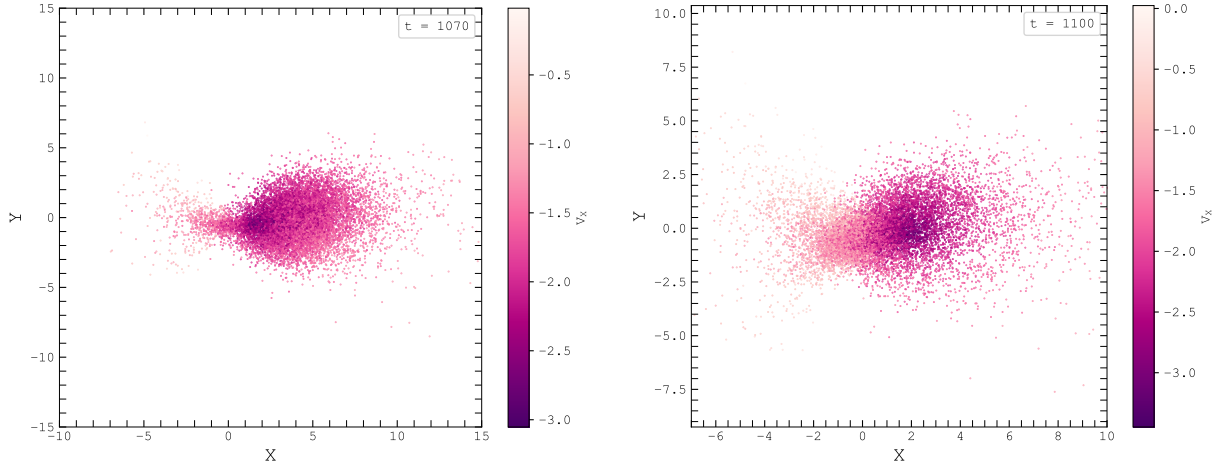


Figure 12

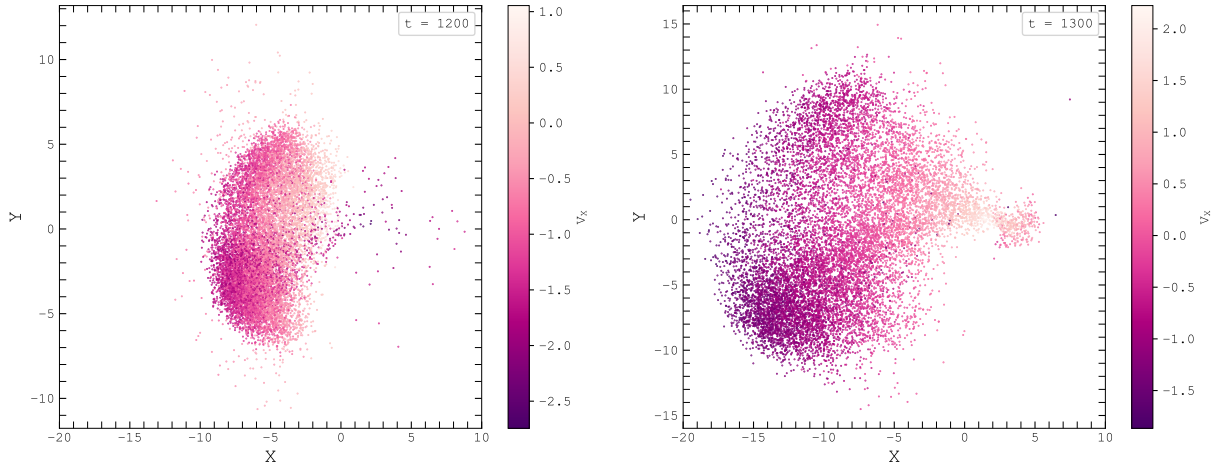


Figure 13. Closeup, xy projections of the disk debris throughout the merger. The color is mapped to the radial velocity component, v_x , showing the complex kinematics of the merger.

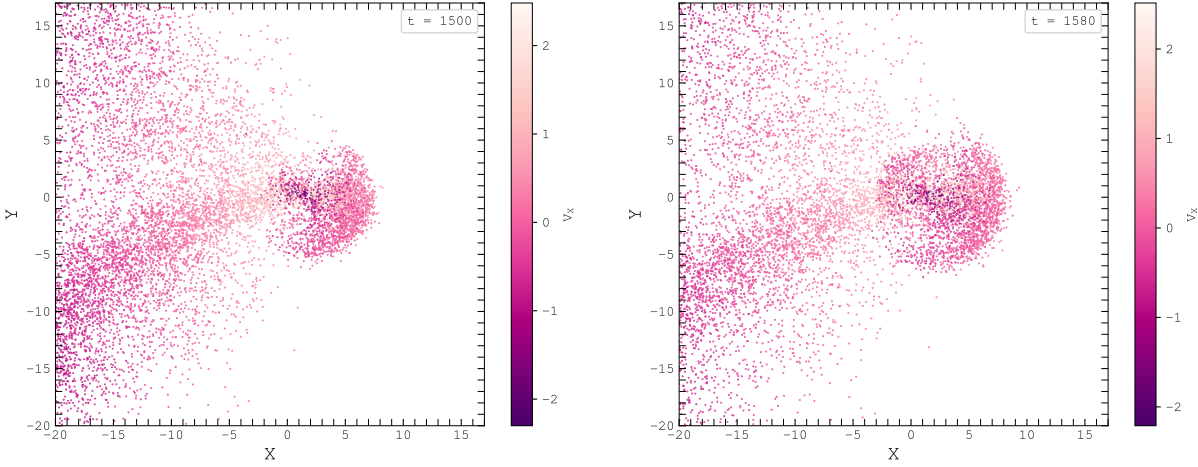


Figure 14. Closeup of the inner core during the merger. The distinct shells of stellar particles looping onto themselves are clearly visible.

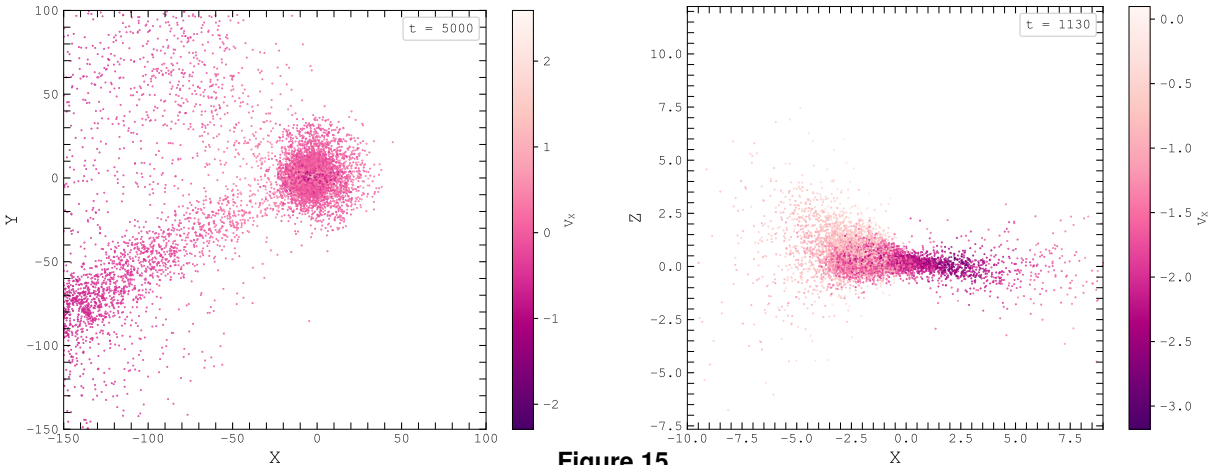


Figure 15

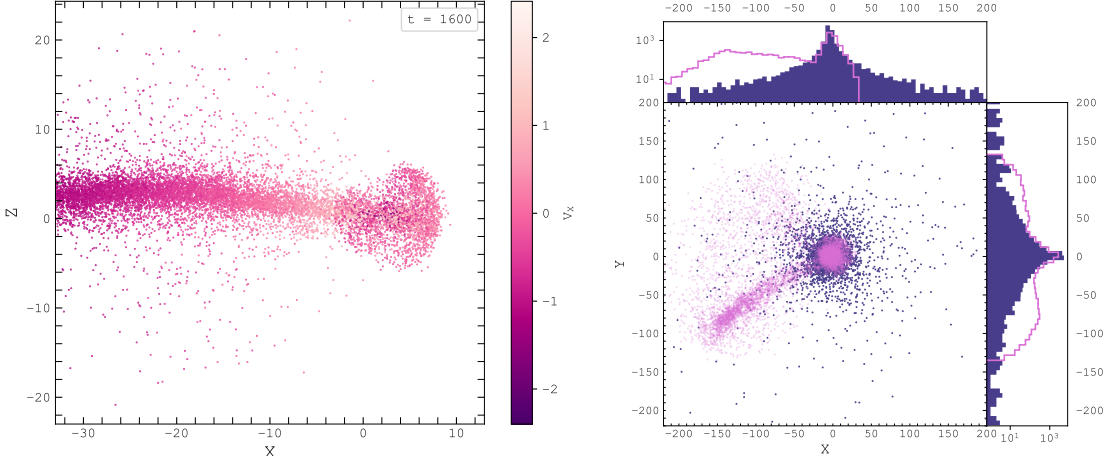


Figure 16. Left panel: xz projection of the merger remnant. Right panel: xy view of the last simulation snapshot with log plots of x and y number density.

Time-series position v. velocity diagrams of simulation 2 are shown in Figure 17 and 18. In Figure 17, the disk is viewed edge-on from the xz plane as the simulation progresses. The line of sight was chosen to be the vector $\|1, 1, 0\|$, or pointing anti-parallel to the direction of travel of the main tail. The undisturbed disk (time 0) is shown in the first panel for reference, with the disk rotation clearly reflected in the phase diagram. At the start of the merging process ($t = 1,120$), the symmetrical nature of the phase diagram becomes more irregular and compressed, with a large velocity dispersion present throughout the disk. The complex and irregular kinematics are clearly seen in the evolution of the phase diagrams, which gradually becomes more elongated and thinner. The tail is clearly seen in the diagrams and shows a lot of evolution between $t = 1,120$, $t = 1,200$, and $t = 1,260$, with the tail's main axis shifting completely to negative velocities. This confirms the tail is traveling in the xy plane towards the line of sight. The positions immediately to the left of the central spheroid at times $t = 1,400$ - $4,000$ also exhibit a more narrow velocity dispersion, which broadens at larger distances. The central spheroid looks very similar to the remnant found in the radial, face-on simulation. Figure 18 shows the xy phase diagrams of the disk along the \hat{z} line of sight vector. These merger remnants are mostly confined to a v_{losz} of zero, which is expected for a merger confined to the xy plane.

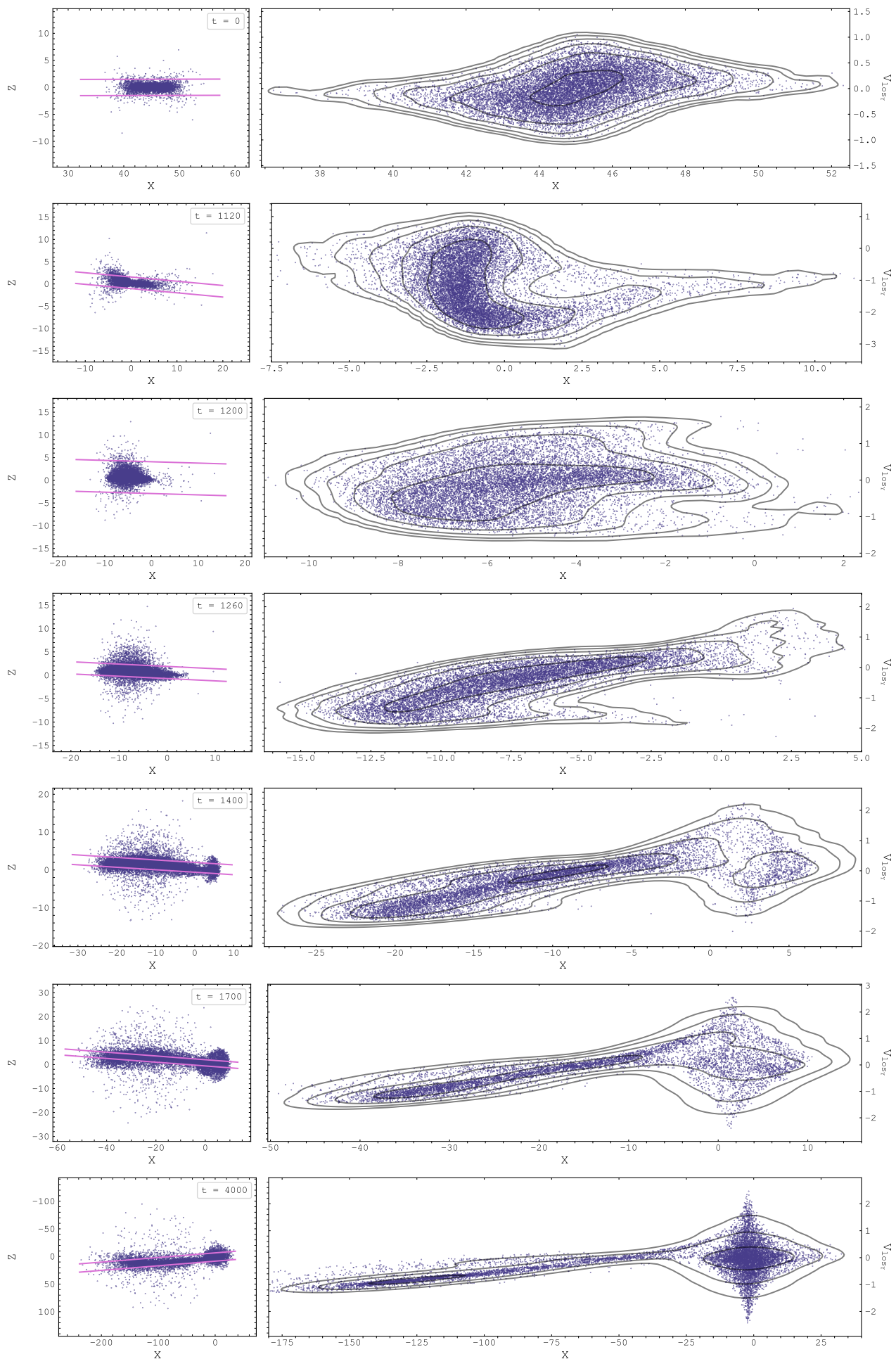


Figure 17. Position v. velocity diagrams of the xz projection of simulation 2 along the line of sight vector $\|1, 1, 0\|$.

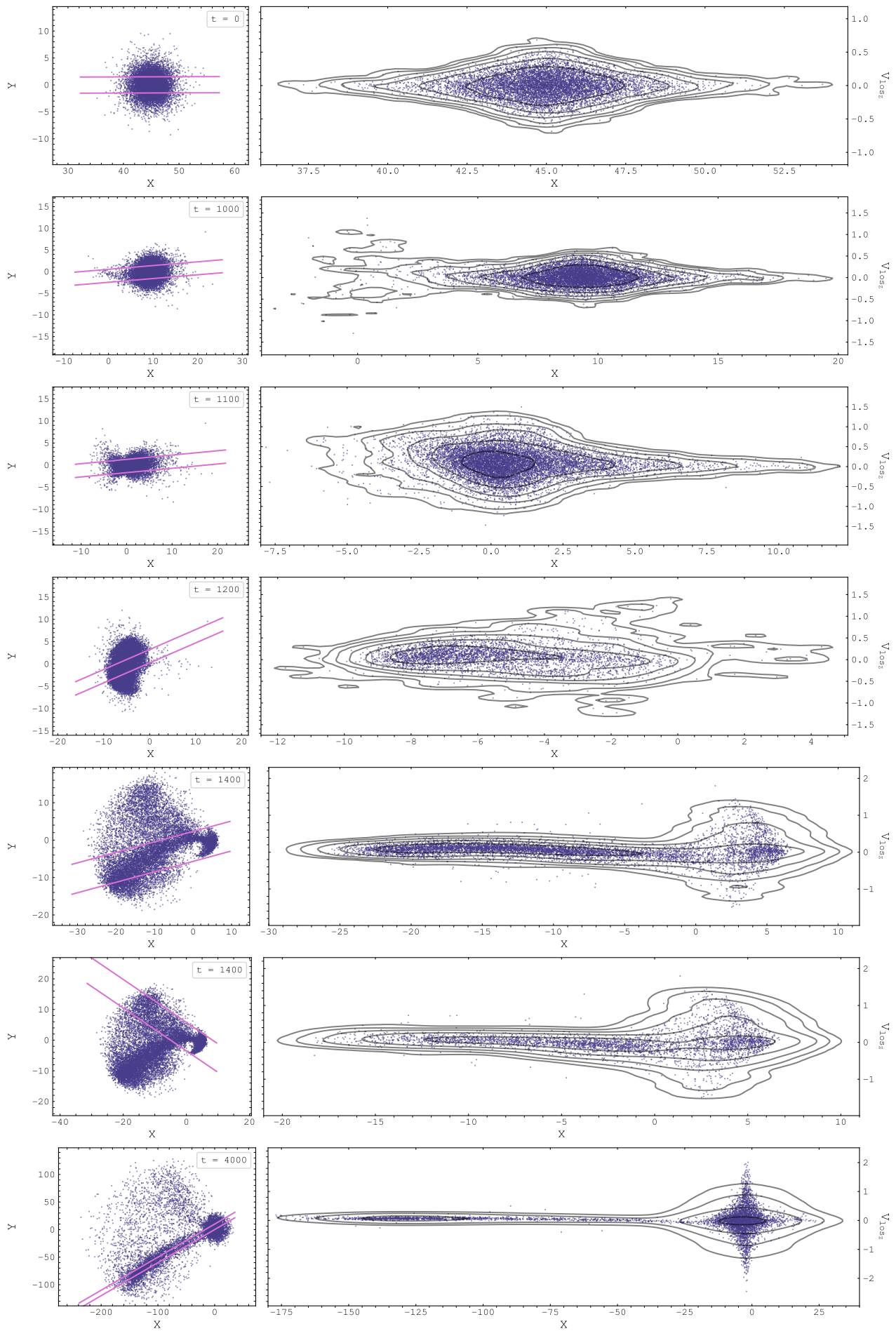


Figure 18. Position v. velocity diagrams of the xy projection of simulation 2 along the \hat{z} line of sight vector.

3.4 Simulation Run 3

The third and final simulation run differed from the first two by having a non-zero impact parameter. The simulation setup was identical to simulation 2, but the perturber galaxy was also given an initial y coordinate of 10 simulation units. The effects of the impact parameter are seen in the final tail ($t = 2,000$), which has rotated counter-clockwise with respect to the tail in simulation 2. Viewed at times 1,250 and 1,450, the tail has completed almost a full 180° rotation about the central core—a property not seen in the fully radial mergers. This implies some of the angular momentum from the disk rotation is kept in the merger remnant, creating loops of debris rotating around the center (see $t = 3,000$). The central spheroid is also much larger and more spherically symmetric, with large shells of stellar particles seen at times 3,000 and 4,240 in Figure 19. Plotting the snapshots on the xz plane (Figure 20) reveals a large range of vertical motion not present in the edge-on simulation. In Figure 21 (left panel), the Energies at different timesteps are plotted on a log-log plot. As expected, the initial disk is much narrower than the analytical Hernquist profile, yet becomes even narrower during the initial collision ($t = 1,300$) before broadening into more smooth distribution. Figure 21 (right panel), displays the final remnant as seen from the xy plane. The number density of the disk particles is much less evenly distributed in the y direction when compared to the final distribution of simulation 2 (Figure 16, right panel), with most of the particles having a negative y coordinate. The density in the x direction however agrees more closely between the two runs. In phase space viewed from yz plane, the remnant is seen rotating almost 180° degrees from times 1,230 to 1,380. The velocity dispersion is initially quite large before compressing into the narrow tail also found in the previous simulation.

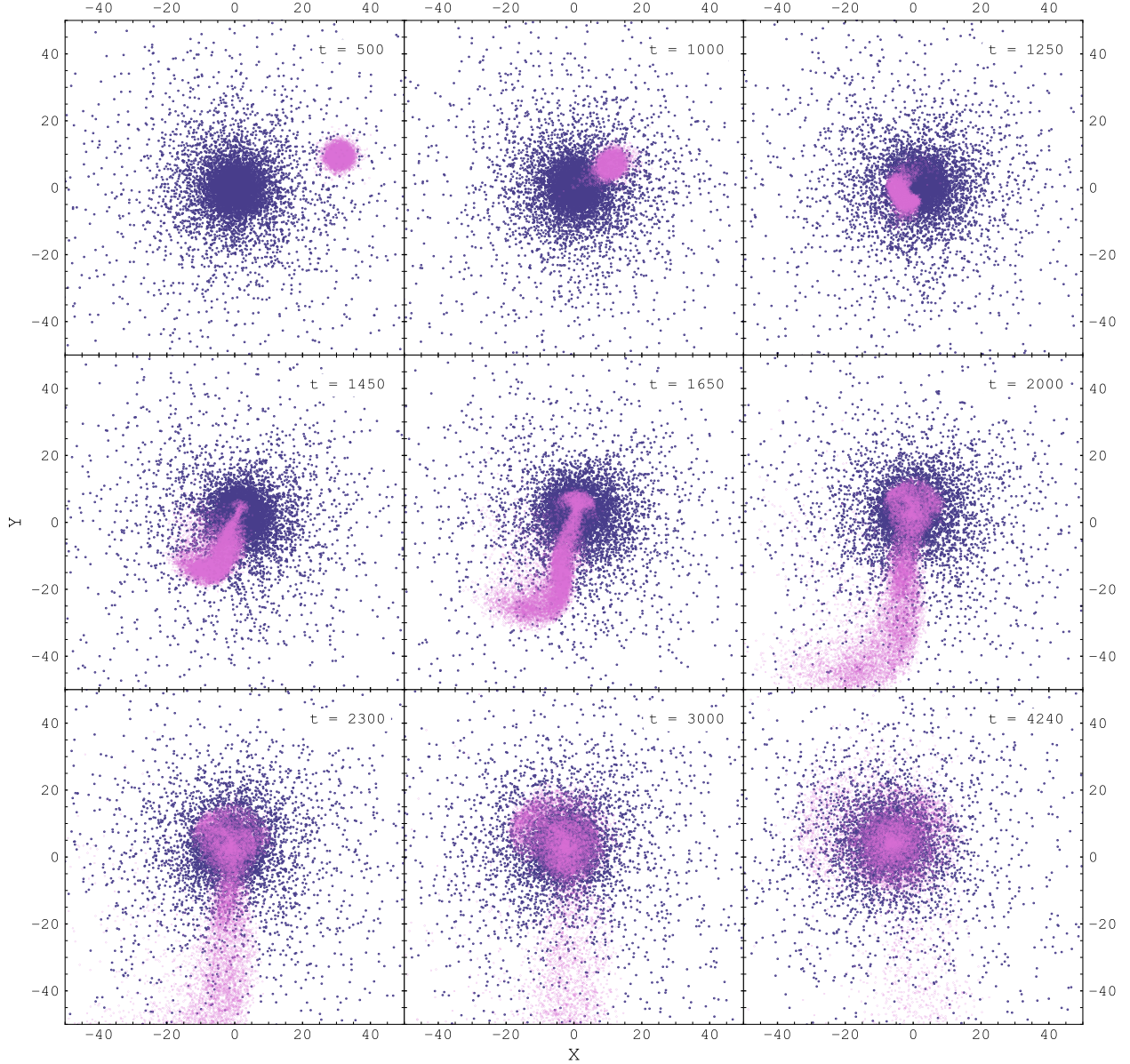


Figure 19. xy projection of the third simulation run from start to finish.

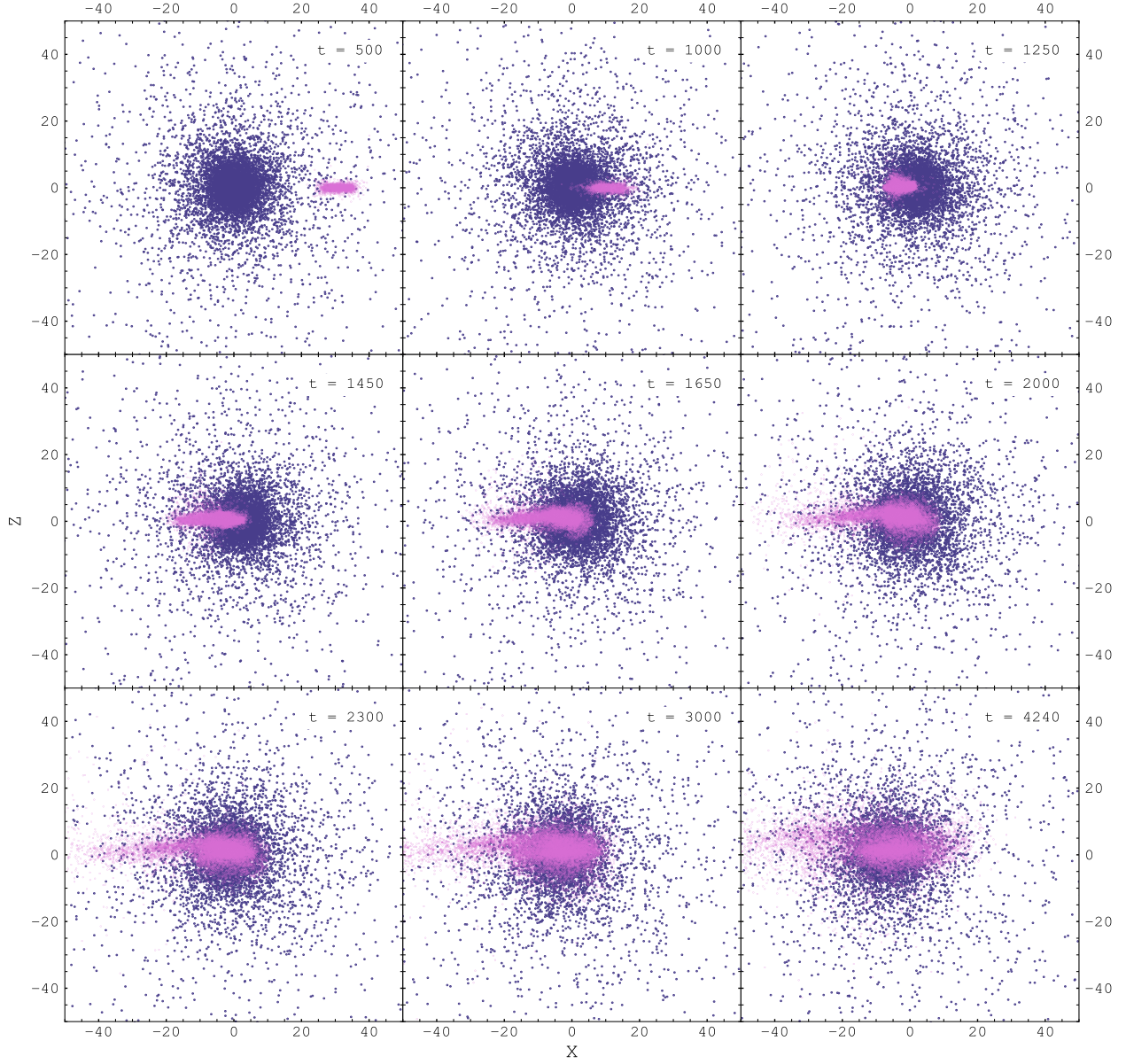


Figure 20. xz projection of the third simulation run. The bulge is much more prominent than in the previous runs.

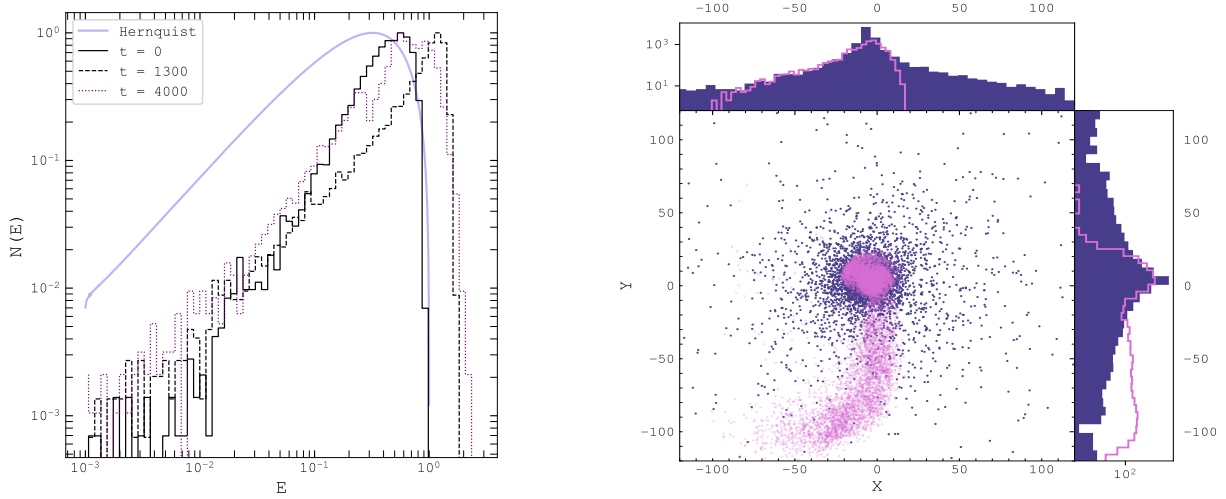


Figure 21. Left panel: $N(E)$ distribution of simulation 3 at different times. Right panel: Final simulation snapshot of simulation 3 with x and y number density histograms plotted.

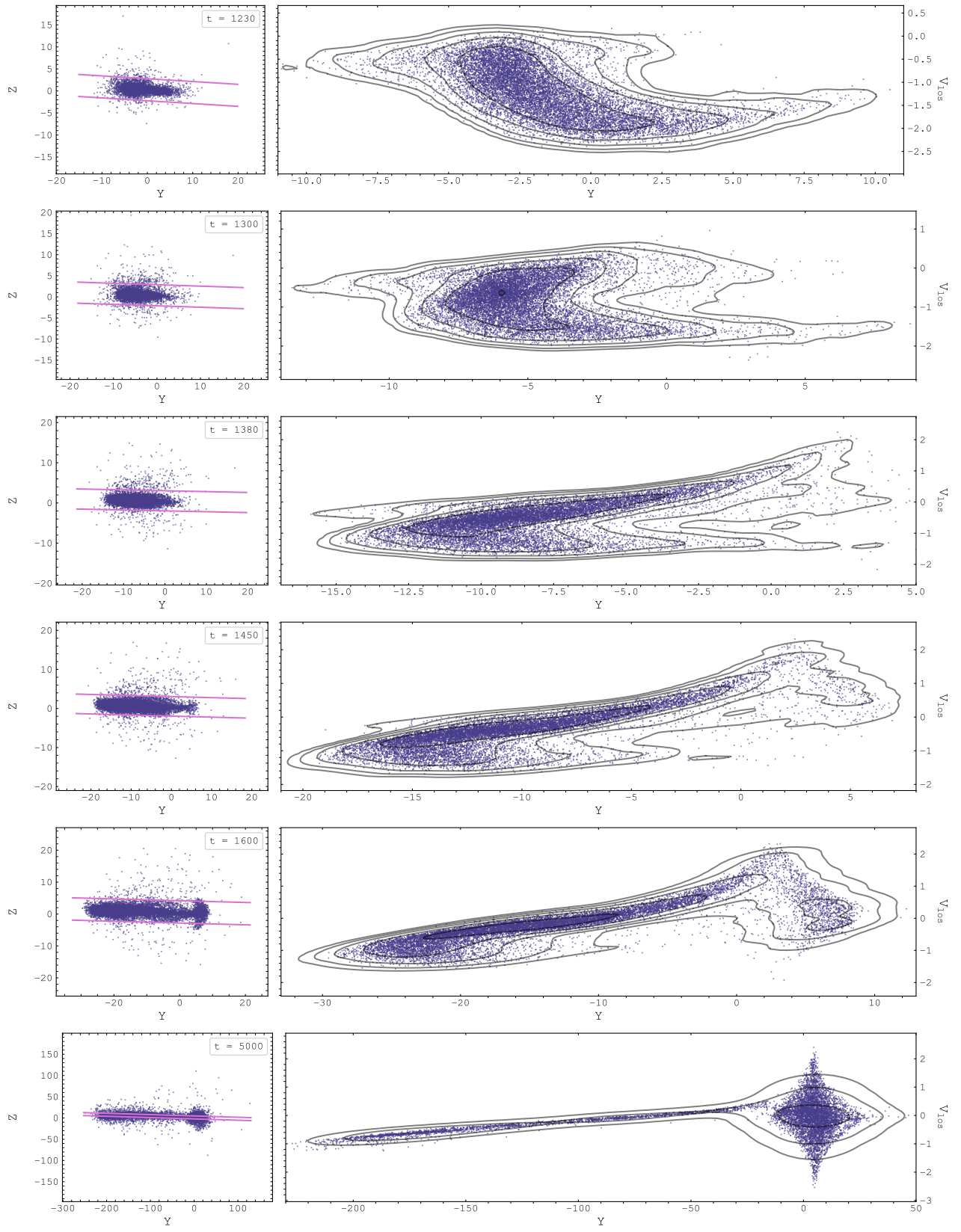


Figure 22. Position v. velocity diagrams of the yz projection of simulation 3 along the line of sight vector $\|1, 1, 0\|$.

4 CONCLUSION

Although far from accurately simulating Fornax A, the simulations having an extremely low particle count, and missing important components such as dark matter, gas, and a central bulge, these simulations offer some insight into the effects of gravity onto collisionless radial mergers. The merger remnants of the radial cases have elongated, continuous distributions similar to the CO distribution seen in Fornax A. The simulations ran in this project are in favor of the perturber merging with Fornax A having a highly radial component, although this needs to be investigated more. Parameter space is very large and there are many more combinations of impact parameters, initial velocities, and disk inclinations to simulate. In the future I hope to continue to optimize the code, such as looking into grid algorithms to support tens of thousands more particles.

5 ACKNOWLEDGMENTS

I would like to thank Professor Jeffrey Kenney and Shashank Dattathri for providing invaluable help in completing this project. This would not have been possible without them. I would also like to thank my Astro Big-Sib Sebastian Monzon for helping me out with running the simulations.

REFERENCES

- Binney, J. and Tremaine, S. (1987). *Galactic Dynamics*. Princeton Series in Astrophysics.
- Dehnen, W. (2001). Towards optimal softening in three-dimensional N-body codes — I. Minimizing the force error. *Monthly Notices of the Royal Astronomical Society*, 324(2):273–291.
- Iodice, E., Spavone, M., Capaccioli, M., Peletier, R. F., Richtler, T., Hilker, M., Mieske, S., Limatola, L., Grado, A., Napolitano, N. R., Cantiello, M., D'Abrusco, R., Paolillo, M., Venhola, A., Lisker, T., Van de Ven, G., Falcon-Barroso, J., and Schipani, P. (2017). The Fornax Deep Survey with VST. II. Fornax A: A Two-phase Assembly Caught in the Act. , 839(1):21.
- Kenney, J.D.P. (2023). Alma co imaging of molecular gas in ngc 1316 (fornax a): I. discrete feature analysis. *placeholder*.
- Lanz, L., Jones, C., Forman, W. R., Ashby, M. L. N., Kraft, R., and Hickox, R. C. (2010). Constraining the outburst properties of the smbh in fornax a through x-ray, infrared, and radio observations. *The Astrophysical Journal*, 721(2):1702.
- Morokuma-Matsui, K., Serra, P., and Maccagni, F.M. (2019). The flickering nuclear activity of fornax a. AA, PASJ, 71, 85.
- NASA, ESA, and STScI/AURA (2005). Hubble space telescope. *placeholder*.
- Richtler, T., Hilker, M., Kumar, B., Bassino, L. P., Gómez, M., and Dirsch, B. (2014). The globular cluster system of ngc 1316 - iii. kinematic complexity. AA, 569:A41.
- Schweizer, F. (1980). An optical study of the giant radio galaxy NGC 1316 (Fornax A). , 237:303–318.
- Vasiliev, E. (2018). AGAMA: action-based galaxy modelling architecture. *Monthly Notices of the Royal Astronomical Society*, 482(2):1525–1544.
- (Binney and Tremaine, 1987) (Dehnen, 2001) (Iodice et al., 2017) (Kenney, J.D.P., 2023) (Lanz et al., 2010) (Morokuma-Matsui, K. et al., 2019) (NASA et al., 2005) (Richtler, T. et al., 2014) (Schweizer, 1980) (Vasiliev, 2018)